Catalysis Today xxx (xxxx) xxx–xxx

Contents lists available at ScienceDirect

Catalysis Today

journal homepage: www.elsevier.com/locate/cattod

Conversion of succinic acid over Ni and Co catalysts

Mabel Rojas[a,b,*], Ximena Zarate[c], Roberto I. Canales[a,b], Ana Belen Dongil[d], Cesar Pazo[b,e], Mario Saavedra-Torres[c], Néstor Escalona[a,b,e,f,*]

[a] Departamento de Ingeniería Química y Bioprocesos, Pontificia Universidad Católica de Chile, Avenida Vicuña Mackenna 4860, Macul, Santiago, Chile
[b] Millenium Nuclei on Catalytic Processes Toward Sustainable Chemistry (CSC), Chile
[c] Instituto de Ciencias Químicas Aplicadas, Theoretical and Computational Chemistry Center, Facultad de Ingeniería, Universidad Autónoma de Chile, Av. Pedro de Valdivia 425, Santiago, Chile
[d] Instituto de Catálisis y Petroleoquímica CSIC, Marie Curie 2, 28049, Madrid, Spain
[e] Facultad de Química y de Farmacia, Pontificia Universidad Católica de Chile, Avenida Vicuña Mackenna 4860, Macul, Santiago, Chile
[f] Unidad de Desarrollo Tecnológico, Universidad de Concepción, Coronel, Chile

ARTICLE INFO

Keywords:
Catalytic hydrogenation
Succinic acid
Biomass
DFT-calculations

ABSTRACT

Liquid-phase hydrogenation of succinic acid (SA) over supported Ni and Co catalysts was investigated at 200 °C and 6 MPa of H_2. Reduced and passivated catalysts with the same surface metal density (2.5 atoms of metal per nm^2 of support) were prepared by incipient wetness impregnation. The catalysts were characterized by X-ray diffraction (XRD), N_2 adsorption, X-ray photoelectron spectroscopy (XPS), temperature-programmed reduction (TPR), CO-chemisorption, and temperature-programmed desorption of NH_3 (TPD-NH_3). The Ni and Co catalysts supported over SiO_2 showed different product distribution, due to the adsorption of the SA over the surface of catalysts, determined by DFT calculations. The Co/SiO_2, Co/SiO_2-Al_2O_3, and Co/Al_2O_3 catalysts showed different product distribution, which was correlated with total acidity from TPD-NH_3 results. In general, the Co catalysts promoted the hydrogenation process; however, the highest total acidity showed by Co/Al_2O_3 also promoted the dehydration process. Finally, the initial rate follows the trend according to the dispersion determined by CO-chemisorption.

1. Introduction

The discovery of the oil industry, in the nineteenth century, generated a source of low-cost fuel that boosted industrialization worldwide [1]. Oil has been not only the main source for liquid fuel but also the basis for most of the chemicals we currently use [2]. However, the increase in global energy demand, the gradual decline in fossil oil reserves, fluctuations in the price of crude oil and mainly the negative impact on the environment have raised the need to develop new energy-efficient processes for the sustainable production of alternative energy sources [1–8]. Due to the above, in recent decades, industries based on renewable resources have been developed for the production of fuel and chemicals, as a replacement for fossil fuels [9]. In this sense, biomass is considered sustainable, neutral in CO_2 emissions, and the most abundant carbon-containing renewable feedstock on the earth [10]. For these reasons, biomass has become an alternative source of fossil raw material for the production of biofuels and renewable chemicals, giving a new concept called biorefinery [9–12].

Lignocellulosic biomass, generally known as agricultural and forestry waste, is the most abundant and renewable natural material worldwide, with an annual production of $150-170 \times 10^9$ tons [10,13]. This type of biomass could be converted into different biofuels, including oxygenated fuels, such as ethanol, butanol, etc., hydrocarbons (alkanes, olefins, and aromatic compounds) and multi-platform chemicals; such as furan, furfural, ketone, levulinic acid, 1,4-diacids, γ-valerolactone, 6-amyl-α-pyrone and phenolic derivatives [8,13–15]. In recent years, the development of technologies to establish successful biorefineries has been actively carried out to replace current petrochemical technologies based on fossil resources [16].

From the biomass, platform molecules can be obtained with interesting carbon-carbon chemical bonds to generate new high value-added chemicals [17,18]. In 2004, the United States Department of Energy (DOE) selected the twelve main platform chemicals that can be produced from biomass [19]. Subsequently, Bozell and Petersen [20] carried out an update of these platform molecules, derived from biomass, considering the top 10 for their production from biorefinery, capable of

* Corresponding authors at: Departamento de Ingeniería Química y Bioprocesos, Pontificia Universidad Católica de Chile, Avenida Vicuña Mackenna 4860, Macul, Santiago, Chile.
E-mail addresses: mnrojas1@uc.cl (M. Rojas), neescalona@ing.puc.cl (N. Escalona).

https://doi.org/10.1016/j.cattod.2020.04.067
Received 31 December 2019; Received in revised form 1 April 2020; Accepted 30 April 2020
0920-5861/

competing economically with the industry of the oil refinery.

Some organic acids have been considered in the DOE, and Bozell and Petersen reports [19,20], because they are easily obtained from biorefinery [21]. Therefore, they have received a lot of attention as platform chemicals. Among them, succinic acid (SA) has been established as a key chemical platform for the bioeconomics era, which has generated a growing industrial interest in its commercialization [16,20,22,23]. SA is one of the few dicarboxylic acids present in the Earth's troposphere and occurs in nature as a metabolite of multiple organisms. As a carboxylic acid, it can participate through intermolecular hydrogen bonding being an important biological building block [24]. For instance, succinate, the anion form of succinic acid is an intermediate in the citric acid cycle, with an important role in the fermentation of sugars, metabolite formation and renewable carbon sources [25]. From an industrial point of view, SA is used in broad industrial fields as an ingredient to stimulate the growth of animals and plants, and as an additive in food and pharmaceutical products, detergents or biodegradable plastics [26].

Among the chemicals of interest, that are generated from the catalytic conversion of SA, are γ-butyrolactone (GBL), 1,4-butanediol (BDO), tetrahydrofuran (THF), fumaric acid, adipic acid, succinamide, acid maleic, maleic anhydride, among others [27–36]. Figure S1, in supporting information, shows the general network of SA conversion. The high value-added chemicals mentioned above have important applications, such as solvents, additives in cosmetics and fragrances, in the synthesis of biopolymers, etc. [27,37,38]. For example, GBL is used as raw material for synthesis N-vinyl pyrrolidone and its corresponding polymer, which is widely used in medicine [27]. In addition, GBL is used as a solvent for fine chemicals and in the pharmaceutical industry [38]. On the other hand, BDO is a versatile raw material that has a wide range of industrial applications [38]. For example, BDO has been used as an organic solvent in the production of adhesives, fibers, and polyurethanes [27,28,39]. Additionally, BDO has received significant attention as a raw material for the production of thermoplastic polymers, such as polybutylene succinate (PBS) and polybutylene terephthalate (PBT) [40]. Finally, THF is used as a monomer for the production of polytetramethylene ether glycol (PTMEG), as a solvent in PVC cement, in pharmaceutical and coating products, or as a reaction medium [27]. THF production has an important global impact due to the 440 thousand tons of this solvent that are produced annually, with an approximate cost of 0.70 − 0.77 USD/Kg [27]. Due to the vast application of the products obtained from the catalytic conversion of SA in the industrial field, it is attractive and beneficial to obtain them from a renewable source such as biomass.

Analyzing the typical catalysts for the conversion of SA, it is observed that the most used active phases have been noble metals (Pd, Ru, among others) and non-noble metals (of higher cost) as Re, mainly due to their highly hydrogenating properties [38,41–48]. For instance, Hong and Song [41] reported the hydrogenation of SA to GBL, over Pd catalysts modifying their acidic density. They determined that the conversion of SA and yield for GBL increased by increasing the acid density of Pd/AX catalysts [41]. Additionally, Hong and Song [44] reported the hydrogenation of SA over Ru-carbon composite (Ru-C) catalysts with different pre-graphitization temperature method. Yield for THF in the hydrogenation of SA increased with decreasing of the ruthenium particle size of Ru–XC catalysts. Thus, ruthenium particle size played a key role in determining the catalytic performance in the hydrogenation of SA to THF over Ru–XC catalysts [44].

SA has been described as a potent agent applied in catalysis to get BDO as mentioned before. In this framework, there are several research studies about transition metals acting as a catalyst. Le and Ebitani explored the direct esterification of SA with phenol in the presence of zeolite catalysts, where the highest yield of diphenyl succinate was achieved over zeolite β in toluene [49]. Abou-Hamdan and Perret evaluated the MoC/TiO_2 catalyst, where GBL was obtained, and more remarkably butyric acid (BA), while intermediates were converted to THF, butanol, BDO and butane [50]. Le and Nishimura found that a fine alloying structure of Cu-Pd with high Cu content is significant to favor the formation of BDO via the ring-opening step of GBL and with good recycling cycles of the catalyst, in contrast with pure Cu or Pd that does not favor the formation of BDO as the primary product [51].

Despite these studies, few of them describe the process of adsorption of SA and metal catalyst under experimental techniques. Humblot mainly described the adsorption of decarboxylated SA and tartaric acid (TA) through several spectroscopic techniques, scanning tunneling microscopy (STM), temperature-programmed desorption (TPD), TPDFTIR, LEED, reflection absorption infrared spectroscopy (RAIRS), over Cu(110) surfaces, showing that particularly to SA, both, monosuccinate and bisuccinate structural forms were found [52]. In the same way, Taheri and Terryn, studied the bonding properties through FTIR and XPS methods of SA, myristic acid, and succinic anhydride molecules with a set of differently pretreated zinc surfaces. This study found that a sufficiently positive potential promoted an interaction between the adsorbates depending on the applied experimental parameters. Particularly, it was confirmed that the anhydride ring opens at the surface due to a reaction with hydroxyl groups and that a high hydroxyl fraction promotes the adsorption of SA molecules with both ending carboxylic groups [53].

In the herein work, different supported Nickel and Cobalt catalysts were prepared and used for the hydrogenation of SA in a batch reactor. The influence of acid sites and metal behavior on catalytic activity was investigated. The structural and surface properties of the catalysts were characterized and correlated with their performances. Additionally, a rigorous computational study was performed to describe the adsorption phenomenon of the substrate on the metal catalysts of Nickel and Cobalt. To achieve this goal, unit cell parameters of the materials were optimized, and slab models were constructed to generate a large number of adsorption configurations of SA over the metallic surfaces. The energetical and structural differences in terms of energy adsorption and interaction SA-slabs conformations were assessed through the evaluation and comparison of the stable adsorption modes of SA onto the catalysts.

2. Materials and methods

2.1. Materials

All the chemical reagents used in this study were obtained commercially: silica (SiO_2), alumina (γ-Al_2O_3, Spheralite (SPH) 501 A), silica-alumina (SiO_2-Al_2O_3, Ketjen HA 100 SP), Nickel(II)nitrate hexahydrate (> 99 %, $Ni(NO_3)_2{\cdot}6H_2O$), Cobalt(II)nitrate hexahydrate (> 99 % $Co(NO_3)_2{\cdot}6H_2O$), succinic acid (> 99 %), succinic anhydride (> 99 %), γ-butyrolactone (99 %), 1,4-butanediol (99 %), tetrahydrofuran (99 %), butyric acid (95 %), propionic acid (95 %), 1-butanol (98 %), ethanol (98 %), propionaldehyde (98 %), 1-propanol (99 %), 2-hydroxytetrahydrofuran (95 %), and dioxane (99 %) were obtained from Merck. The gases used were H_2 (99.995 %, Linde), N_2 (99.995 %, Linde), He (99.995 %, Linde), 10 % O_2/N_2 (certified mixture grade, Linde), 5% H_2/Ar (certified mixture grade, Linde), and NH_3 (99.5 %, Indura). All chemicals in this work were used without further purification.

2.2. Catalyst preparation

The supported Cobalt and Nickel catalysts were prepared by incipient wetness impregnation of an aqueous solution of $Co(NO_3)_2{\cdot}6H_2O$ or $Ni(NO_3)_2{\cdot}6H_2O$ over three different supports (SiO_2 S_{BET} = 355 $m^2\,g^{-1}$, γ-Al_2O_3 S_{BET} = 327 $m^2\,g^{-1}$ and SiO_2-Al_2O_3 S_{BET} = 365 $m^2\,g^{-1}$). Previously, the supports were ground and sieved to obtain a maximum particle size of 150 μm. After impregnation, the samples were kept at room temperature for 24 h and then dried at 110°C for 12 h.

The Ni/SiO_2 catalyst was calcined at 550 °C (ramp of 10 °C min^{-1})

for 4 h and reduced in a quartz reactor tube placed inside an electrical furnace under a flow of H_2 (60 mL min^{-1}) at 450 °C (ramp rate of 10 °C min^{-1}) for 3 h. In the case of Co/X (X = SiO_2, γ-Al_2O_3 and SiO_2-Al_2O_3) catalysts, they were calcined at 500 °C (ramp of 10 °C min^{-1}) for 4 h and reduced in the same system of Ni/SiO_2 catalysts, at 500 °C (ramp rate of 10 °C min^{-1}) for 3 h.

The samples were cooled down to ambient temperature under N_2 (60 mL min^{-1}). They then were passivated under a flow of 5% O_2/N_2 (60 mL min^{-1}) through two processes: (1) for 1 h immersed in a liquid nitrogen/isopropanol slurry bath and (2) for 1.5 h at ambient temperature.

Finally, the following catalysts were obtained: Ni/SiO_2, Co/SiO_2, Co/SiO_2-Al_2O_3, Co/Al_2O_3 with the same surface metal density (2.5 atoms per nm^2 of support).

2.3. Catalyst characterization

X-ray diffraction (XRD) patterns of the catalysts were acquired in the 2θ range between 4° and 90° with a step of 0.04°/s using a Polycristal X'Pert Pro PANalytical diffractometer with Ni-filtered Cu Kα radiation (λ = 1.54 Å) operating at 45 kV and 40 mA. Prior to the experiments, the samples were reduced using the same experimental conditions as those of the reaction tests.

Nitrogen adsorption-desorption isotherms of the supports and reduced catalysts were obtained at -196 °C using a Micromeritics 3-Flex instrument to evaluate the BET surface area (S_{BET}), total pore volume (V_p) and average pore diameter (d_p). The samples were previously degassed under vacuum at 300 °C for 4 h in a nitrogen flow, under vacuum using a Micromeritics SmartVacPrep instrument. The surface area was calculated from the adsorption branch of the isotherms in the range of $0.05 \leq P/P_0 \leq 0.25$ using the Brunauer-Emmett-Teller (BET) theory and V_p was recorded at $P/P_0 = 0.99$. The average pore diameter was estimated from the desorption branch using the BJH method [54].

XPS measurements were performed with an energy analyzer (PHOIBOS 150 9MCD, SPECS GmbH) using non-monochromatic Al radiation (200 W, 1486.61 eV). The samples were pelletized and reduced using the same experimental conditions as those of the reaction experiments. The samples, in the reduction reactor, were transferred to a glove box and placed in the sample holder that was quickly transferred to the outgassed chamber. Before the experiments, samples were outgassed *in-situ* for 24 h to achieve a dynamic vacuum below 10^{-10} mbar. The binding energy (BE) was measured by reference to the C 1s peak at 284.6 eV, with an equipment error of less than 0.01 eV in the energy determinations.

Chemisorption uptakes of CO were measured at 35 °C using a Micromeritics 3-Flex instrument. Typically, 30 − 50 mg of passivated catalyst was first degassed at 110 °C (10 °C min^{-1}) for 30 min and then reduced in-situ to the conditions of each metal (Ni and Co) described before. The first adsorption isotherm was collected between 50 and 450 mmHg. The system was evacuated for 1 h to remove weakly adsorbed CO, and then a second isotherm was recorded. CO uptake was finally calculated from the difference between the two adsorptions isotherms.

H_2-Temperature Programmed Reduction (TPR) of the calcined catalysts was performed using a Micromeritics 3-Flex instrument coupled with a mass spectrometer (cirrus 2, MKS Spectra Product). Typically, 30 − 40 mg of the catalyst was loaded in a U-shaped quartz reactor and dried in flowing He (50 mL min^{-1}) at 110 °C for 0.5 h to remove any weakly retained moisture. Subsequently, H_2-TPR was performed from 50 °C to 900 °C at a heating rate of 10 °C min^{-1} in a stream of 10 % H_2/Ar (50 mL min^{-1}). The effluent gas was passed through a cold trap filled with a mixture of isopropanol and liquid nitrogen to remove water vapor before entering the TCD detector. The products formed during the reduction process were also monitored in parallel by a mass spectrometer fragments m/z of 15, 28, 44, corresponding to CH_4, CO, and CO_2. The H_2O signal (m/z = 18) was also monitored to ensure that the complete removal of water occurred. The amount of H_2 consumed per gram of catalyst sample was calculated from integral of the area under the TCD signal previously calibrated by the reduction of CuO (Micromeritics) as reference.

NH_3-Temperature Programmed Desorption (TPD) of reduced-passivated catalysts was performed using a Micromeritics 3-Flex instrument coupled with a mass spectrometer (cirrus 2, MKS Spectra Product), to obtain the acidity of the catalysts. The calcined catalysts (30 − 50 mg) were reduced in situ at the same conditions of each metal (Ni and Co) described before, then pretreated in flowing He (50 mL min^{-1}) at 110 °C for 0.5 h, and then saturated with NH_3 using He (50 mL min^{-1}) as a carrier gas. The samples were purged with He for 0.5 h to remove physically adsorbed NH_3 and then cooled to ambient temperature in He. Once the baseline was restored, NH_3-TPD was performed at a heating rate of 10 °C min^{-1} up to 900 °C in flowing He (50 mL min^{-1}). The amount of NH_3 desorbed per gram of catalyst was calculated from ammonia mean calibrated areas, an ammonia TPD analytical area.

2.4. Catalytic test

The hydrogenation of SA was carried out in a 300 mL stirred-batch autoclave setup (Parr Model 4566) at 200 °C and under a hydrogen pressure of 6 MPa for 6 h. In a typical run, 0.800 g of succinic acid (0.085 mol L^{-1}) dissolved in 1,4-dioxane (80 mL) was introduced into a stainless-steel reactor. These mixtures, with 100 mg of the dried catalysts were loaded into the reactor, purged with a continuous flow of nitrogen (99.995 %, Linde) for 10 min to evacuate air from the system. Still under N_2 atmosphere, the reactor was heated to the reaction temperature of 200 °C under magnetic stirring. Hydrogen was introduced to adjust the pressure to 6 MPa, which was kept constant during the experiment. Aliquots of around 0.5 mL were periodically withdrawn during the reaction. The reaction products were quantified by gas chromatography (Shimadzu, model 2010) equipped with a Flame Ionization Detector (FID) connected to a capillary column ((14 %-Cyanopropyl-phenyl)-methylpolysiloxane (60 m × 0,25 mm ID; 0,25 mm)). The products were identified by their retention time in comparison with available standards.

The composition of the vapor-liquid equilibrium of the binary system hydrogen + 1,4-dioxane was calculated with PC-SAFT [55] at 200 °C and 6 MPa to estimate an approximate amount of hydrogen in the liquid phase. Pure component parameters for hydrogen were reported by Gross and Sadowski [55], and for 1,4-dioxane were adjusted in this work from experimental density and vapor pressure data obtained from the NIST ThermoData Engine database retrieved from Aspen Plus®. PC-SAFT pure component parameters are reported in Table 1. A binary interaction parameter (k_{ij} = - 0,134714) was adjusted from experimental binary vapor-liquid equilibrium data of hydrogen + 1,4-dioxane found in literature [56]. Finally, the compositions of the vapor-liquid equilibrium were calculated using the aforementioned parameters at 200 °C and 6 MPa. Thus, the mole fraction of hydrogen in the liquid phase is estimated as 0.0295 (hydrogen/succinic acid ratio is 3.5) and in the vapor phase as 0.7937.

The specific rate r_s (mol g_{cat}^{-1} s^{-1}) was calculated from the initial slope of the plot of SA conversion as a function of time, according to the Eq. (1).

$$r_s = \frac{[b \times n]}{m} \quad (1)$$

Table 1
Pure component PC-SAFT parameters used in the calculations.

	Hydrogen	1,4-dioxane
m	0.8285	2.99933
σ (Å)	2.9729	3.36189
ε/k (K)	12.53	274.743

where b is the initial slope of conversion vs. time plot (s^{-1}), n is the initial moles of succinic acid in the solution (mol), and m the amount of catalyst (g). The conversion of SA (X_{SA}) was calculated from Eq. (2).

$$X_{SA} = \frac{n_{SA}^{0} - n_{SA}^{i}}{n_{SA}^{0}} \times 100 \quad (2)$$

where n_{SA}^{0} is the initial moles of succinic acid in the solution (mol) and n_{SA}^{i} is the moles of succinic acid at time *i* (mol). The product selectivity was calculated, according to Eq. (3).

$$Selectivity\,(\%) = \frac{n_{productj}}{n_{SAconverted}} \times 100 \quad (3)$$

where $n_{productj}$ is the moles of product j (mol) and $n_{SAconverted}$ is the moles of SA converted (20 %). The average turnover frequency (TOF, min^{-1}) was calculated from the specific rate r_s and considering the H_2 uptake, according to Eq. (4)

$$TOF = \frac{r_s}{CO_{uptake}} \quad (4)$$

where r_s was previously obtained, and CO uptake was obtained from CO chemisorption. Repeated runs at the same conditions were performed to ensure the satisfactory reproducibility of the data.

2.5. Computational modeling

The interaction between succinic acid and Cobalt and Nickel catalysts was modeled through the adsorption under periodic model. Succinic acid presents considerable torsional flexibility with two diprotic groups which can stabilize some conformers of the molecule via hydrogen bonds, and have been described structurally through several studies [57,58]. For this study, four of the most stable and isoenergetic conformers were selected from the study of Vgot and Shishkov [57], who shows that represents 96 % of mole fractions of succinic acid (according to free energy calculations); these conformers are shown in Fig. 1. However, due to structures I and II represent over 60 % of mole fractions of succinic acid and that those conformers are relatively similar to III and IV, only I and II were adsorbed on the materials. Both conformers were reoptimized under a discrete DFT method (B3LYP/6-311 g(d,p)), showing no structural differences between the reported geometries, remaining a little relative energy difference between them (0.16 eV). These conformers also have been optimized according to the periodic methods, without relevant alterations in their structural parameters.

According to the crystal experimental data obtained as well as taking into account that (111) close-packed surface shows the highest number of active sites and is stable, Co(111) and Ni(111) under FCC were theoretically simulated in this study. Unit cell parameters were optimized using 20 k-points, obtaining a = 3.468 Å (exp = 3.544 Å) for cobalt and a = 3.5153 Å (exp = 3.5249 Å) for nickel, showing a good agreement between calculated and the experimental ones [59,60]. Using these cell parameters, slabs of Co(111) and Ni(111) were modeled as 4 × 4 periodic unit cells with 4 layers. The bottoms layer of the slabs was not allowed to relax and kept the bulk positions, allowing to simulate the top three as FCC layers. An isolation space of 14 Å in the cells was used, where the succinic acid has been placed to assess the adsorption process. For both metals, the adsorbate was initially located at 2.5 Å from the surface (*i.e* perpendicular distance between the adsorbate atom and the metal atom), according to Figure S3, in supporting information. Initial configurations consisted of possible adsorption modes between the atom groups of the adsorbate and metal adsorption sites over the surface (*i.e.* bridge, top, hollow HCP, hollow FCC) according to Figure S2, in supporting information. Specifically, to get results about the most favorable adsorption positions of succinic acid over metal surfaces, multiple models for these two conformers were made. Five key chemical groups of succinic acid were considered: O1, O3, O1-O3, C4-C5, O1-O8 (see Figure S4). Therefore, multiple combinations were considered, and some other groups of the molecule were discarded by similarity or symmetry.

Computations were performed using the Quantum Espresso 6.4 package [61,62], with the Generalized Gradient Approximation (GGA) functional Perdew-Burke-Ernzerhof (PBE) [63] and Quantum-Espresso ultrasoft pseupotentials [64], with energy cutoff of 45 Ryd. Multiple adsorption configurations were optimized at gamma point, selecting the most stables samples to evaluate them energetically under a 3 × 3 × 1 k-points grid. Finally, the adsorption energy of the complexes was determined as $E_{ads} = E_{(SA\text{-}metal)} - E_{(metal)} - E_{SA)}$.

3. Results and discussion

3.1. Catalysts characterization

The XRD patterns of the passivated catalysts are plotted in Fig. 2. The peaks at 2θ = 22.7° and 66.8° could be ascribed to the diffraction peaks of SiO_2 and (003) planes of γ-Al_2O_3 supports, respectively [65].

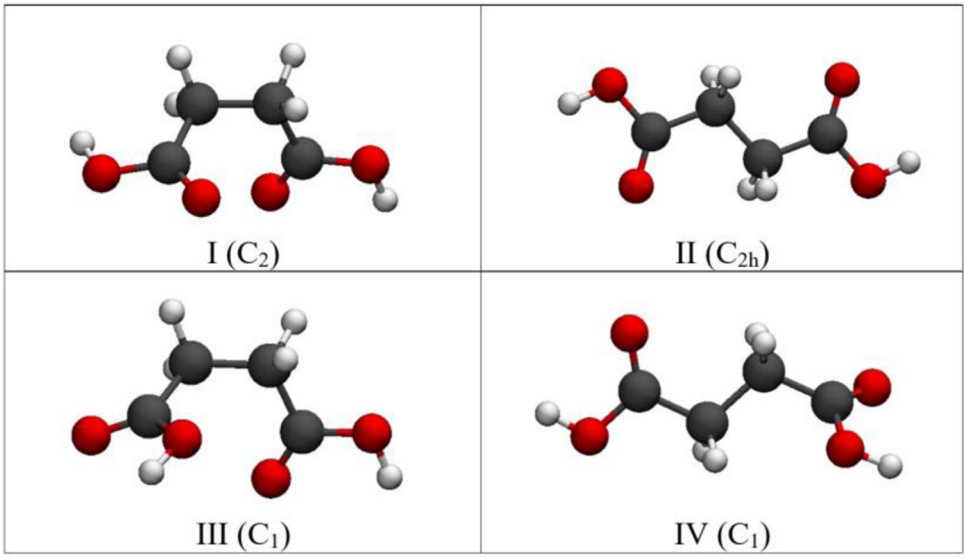

Fig. 1. Most stable conformers of Vgot and Shishkov representing 96 % of succinic acid total mole fraction. I and II are the most representatives (with a 60 %) and were taken in this study.

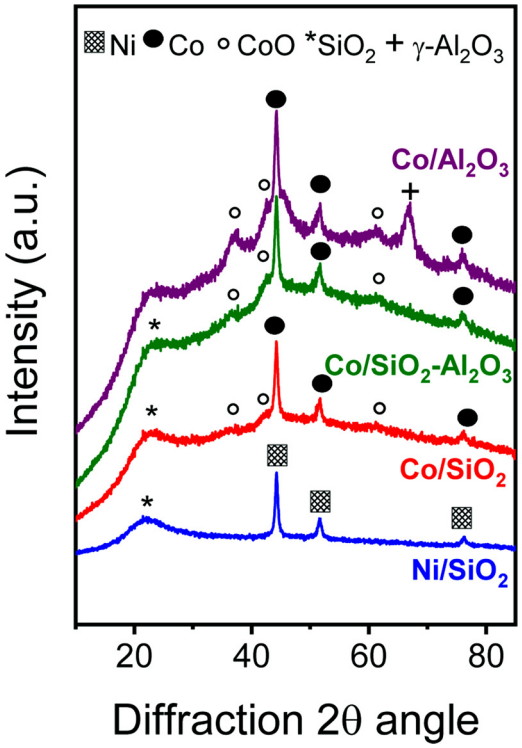

Fig. 2. XRD spectra of difference passivated supported catalysts.

The peaks at 2θ = 44.3°, 51.6° and 76.3° assigned to the diffraction of (111), (200), and (220) planes of metallic Ni, confirm the presence of metallic Ni in the reduced catalyst [66]. The peaks at 44.2°, 51.6°, and 75.9° could be ascribed to the diffraction of (111), (004) and (220) planes of metallic Co, confirming the presence of metallic Co in the reduced catalysts [66]. Additionally, peak at 2θ = 37.1°, 42.3°, and 61.3° in the case of Co-based catalyst, could be ascribed to the CoO species [66], which could be attributed to Co oxide species that are interacting with support together with the oxidation layer from passivation process. The Co-based catalysts exhibited the fcc structure, structure used in DTF studies. Unfortunately, the particle size from Scherrer equation was no calculated for Co/support catalysts, due to the fact that CoO species affect the Co metallic XRD patterns.

The N_2-sorption isotherms obtained for all the catalysts and the supports are shown in Figure S5, in supporting information. All the supports and their corresponding metal catalysts exhibit a type IV isotherm, typical of mesoporous materials, according to IUPAC classification [54]. The SiO_2 and SiO_2-Al_2O_3 supported catalysts show a well-expressed type H1 hysteresis loop, indicative of the presence of cylinder-shaped pores of rate constant cross-section [67]. In the case of γ-Al_2O_3 supported catalyst, the hysteresis loop falls within type H3, associated with slit-like pores [54].

The BET specific surface area (S_{BET}), total pore volume (V_p) and pore diameter (d_p) of the supports and reduced-passivated catalysts are summarized in Table 2. The surface areas of the supports are in accordance with reported values [54] and ranged from 327 to 365 $m^2 g^{-1}$, while the primary pore diameters estimated from the maximum in the BJH pore size distribution varied from 14.3 to 9.5 nm. The Ni/SiO_2 catalyst has a lower surface area than its comparable Co/SiO_2 counterpart.

Comparing the S_{BET} values of Co catalysts (Table 2), Co/SiO_2-Al_2O_3 and Co/Al_2O_3 show lower S_{BET} value, indicating the preferential deposition of the Co metal in the pores of SiO_2-Al_2O_3 and Al_2O_3 supports. These results suggest a partial pore blockage of supports.

The surface element compositions of reduced-passivated catalysts were determined by XPS. Fig. 3 shows the Ni 2p and Co 2p XPS spectra.

Table 2
Textural properties of the supports and catalysts obtained from nitrogen physisorption measurements.

Catalyst	Nominal loading (%w/w)	S_{BET} ($m^2 g^{-1}$)	V_p ($cm^3 g^{-1}$)	d_p (nm)
SiO_2		355	1.27	14.3
Ni/SiO_2	8.0	281	1.01	13.8
Co/SiO_2	8.0	314	1.11	13.7
SiO_2-Al_2O_3		365	0.60	9.5
Co/SiO_2-Al_2O_3	8.2	179	0.32	13.8
γ-Al_2O_3		327	0.43	13.9
Co/Al_2O_3	7.4	210	0.38	13.4

Table 3 summarizes the binding energies (BE) and their relative proportions (shown in parentheses). As can be seen in Fig. 3, Ni/SiO_2 catalyst exhibited binding energies at 852.1 and 856.4 eV corresponding to Ni° ($2p_{3/2}$) and Ni^{2+} ($2p_{3/2}$) respectively, suggesting the presence of both metallic Ni and NiO species on the surface of support [66,68] and no obvious satellite peak is observed in Ni region. Additionally, Co-based catalysts displayed several contributions in the $2p_{3/2}$ region. Co/SiO_2 catalyst exhibited peaks with maxima at binding energies of 778.0 and 781.5 eV attributed to Co° and Co^{2+} in CoO, respectively, as the intense satellite peak also confirm [69–71]. Similar behavior was exhibited by Co/SiO_2-Al_2O_3 and Co/Al_2O_3 samples. The absence of contribution at 780 and 782 eV suggest that neither Co_2O_3/Co_3O_4 or $CoAl_2O_4$ phase were formed in agreement with the XRD profile. The highest binding energy at which Co° appears in Co/Al_2O_3 seems to be in accordance with the strongest metal support interaction over alumina.

The fractions of metal oxidation states, given in parenthesis in Table 3, show that M^0 (Ni and Co metal) species were the dominant surface phase present in all catalysts. Nevertheless, Co^{2+} was present in higher quantities on the surface of Co/Al_2O_3 catalyst, which could be due to the strong interaction between CoO species and the support.

Table 3 summarizes the metal/support (M/X) surface atomic ratios from the XPS spectra of the catalysts. Comparing the Co-based catalysts (Table 3), it is observed that Co/SiO2 showed the highest proportion of metal content (55). Conversely, Co/Al_2O_3 displayed the lowest proportion metal content (25) and the highest M/X surface atomic ratio, while Co/SiO_2-Al_2O_3 catalyst exhibited the lowest M/X surface atomic ratio.

The H_2-TPR analysis was used to determine the nature of the species present in the catalysts and provide some insights into the metal-support interactions. Fig. 4 shows the H_2-TPR profiles of the calcined catalysts. For Co metal catalysts, at least two H_2 consumption peaks (T_{red1} and $T_{red\ 2}$) are observed, due to the typical two-stage reduction of supported Co oxide and Co metal (Co_3O_4 → CoO → Co) [72]. The reduction temperatures of the supported Co catalysts are different owing to the interactions between the supports and the Co species. Co/Al_2O_3 was the most difficult to reduce as reflected in the highest T_{red1} peak at 365 °C, T_{red2} at 644 °C and a weak peak at 865 °C. It has been reported that T_{red2} is associated mainly with the reduction of CoO [54,72]. Additionally, the broad reduction peak at 865 °C could be attributed to the strong interaction of CoO with γ-Al_2O_3 support [72], in agreement with XRD results.

In the case of Co/SiO_2 and Co/SiO_2-Al_2O_3 catalysts, they showed four T_{red}. These could be due to the presence of different types of CoO species that are interacting strongly with the supports, in accordance with high values of proportion metal content obtained by XPS. In summary, the metal-support interaction of the cobalt catalysts decreases in the following order: γ-Al_2O_3 > SiO_2-Al_2O_3 > SiO_2, in agreement with previous reports [54].

In the case of Ni/SiO_2 catalyst, two H_2 consumption peaks (T_{red1} and $T_{red\ 2}$) could be observed. The T_{red1} peak at 356 °C, usually assigned to the reduction of NiO clusters that are interacting with the support [73].

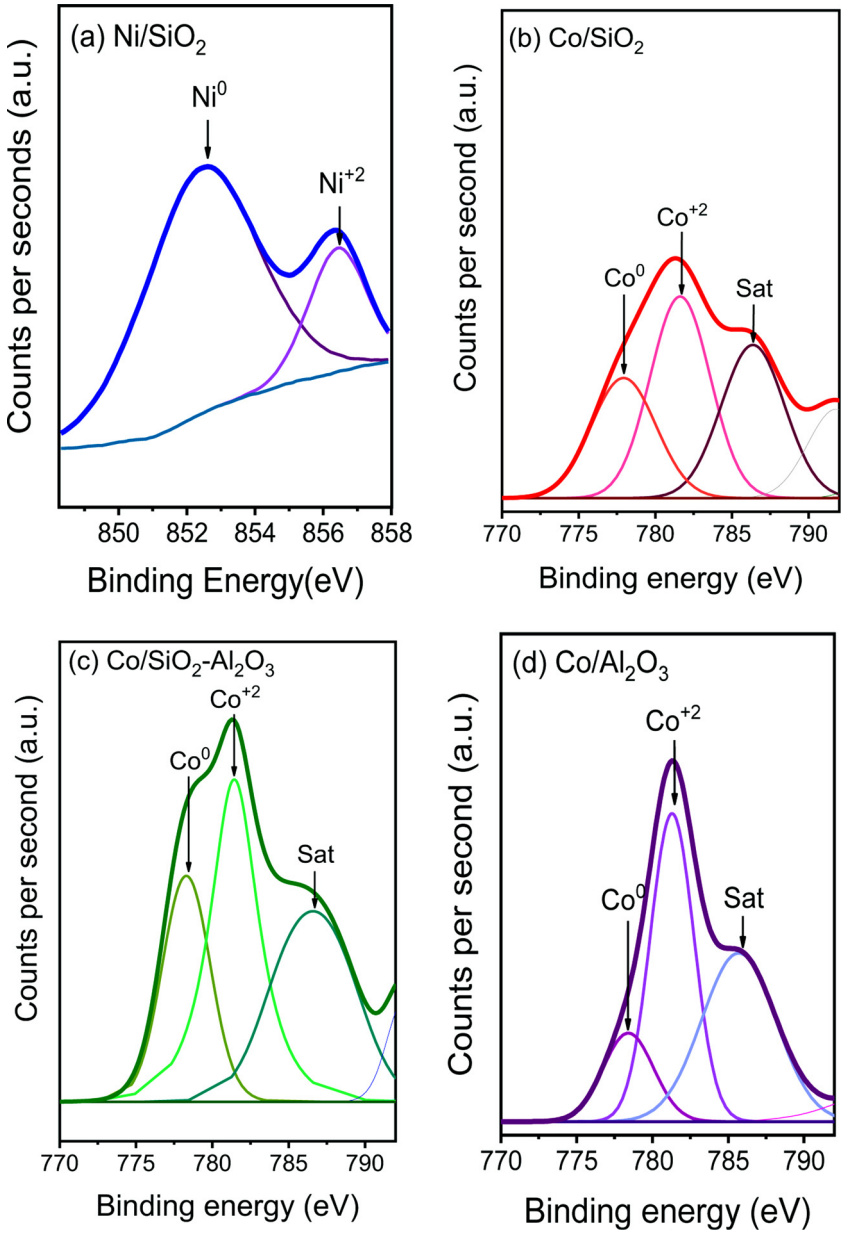

Fig. 3. $2p_{3/2}$ core level spectra of reduced passivated supported (a) Ni/SiO_2, (b) Co/SiO_2, (c) Co/SiO_2-Al_2O_3 and (d) Co/Al_2O_3 catalysts.

Table 3
Binding energy (BE) and atomic ratios of reduced catalysts (M/X = metal/support) and supports (Al/Si = γ-Al_2O_3/SiO_2), obtained from XPS analysis.

Catalyst	Binding energy (eV)		Surface atomic ratio M/X	Support atomic ratio Al/Si
	M^0	M^{2+}		
Ni/SiO_2	852.1 (79)	856.4 (21)	0.014	–
Co/SiO_2	778.0 (55)	781.5 (45)	0.019	–
Co/SiO_2-Al_2O_3	778.1 (38)	781.5 (62)	0.012	0.448
Co/Al_2O_3	778.2 (25)	781.3 (75)	0.027	–

Additionally, the T_{red2} peak at 440 °C is observed; this could be attributed to the same reduction of NiO clusters. It has been reported that the presence of a broad reduction peak between 300 − 700 °C corresponding to the strong interactions of the Ni with SiO_2 support [74].

On the other hand, the Ni/SiO_2 presents the higher H_2 consumption following than Co catalysts, such as those shown in Table 4. This result suggests that the Ni catalyst presents the highest reduction extend, according to XPS results. In the case of Co/support catalysts, the highest H_2 consumption was present for Co/Al_2O_3 following by Co/SiO_2 and Co/SiO_2-Al_2O_3 catalysts. This trend suggests that the Cobalt is easier to reduce over γ-Al_2O_3 than over SiO_2 and SiO_2-Al_2O_3, in agreement with XPS results.

Additionally, Table 4 summarizes the CO uptake, metal dispersion, and the crystal size values obtained by CO chemisorption. This table shows that Ni/SiO_2 displayed both the higher CO uptake and metal dispersion and a smaller crystal size than the Co/SiO_2 catalyst, suggesting that the Ni species displayed a higher dispersion, as opposed to the XPS results. The Co/support catalysts show that Co/SiO_2 has both the higher CO uptake and metal dispersion, followed by Co/Al_2O_3 and Co/SiO_2-Al_2O_3 catalysts. The lowest Co dispersion displayed by Co/SiO_2-Al_2O_3 is in agreement with XPS and S_{BET} values. However, the XPS results suggested that Co/Al_2O_3 has a higher cobalt surface distribution than Co/SiO_2 in opposite with CO chemisorption. This difference result observed between CO chemisorption and XPS results could be attributed to that metal and oxide species are located inside of mesoporous materials, which are affecting the XPS analysis.

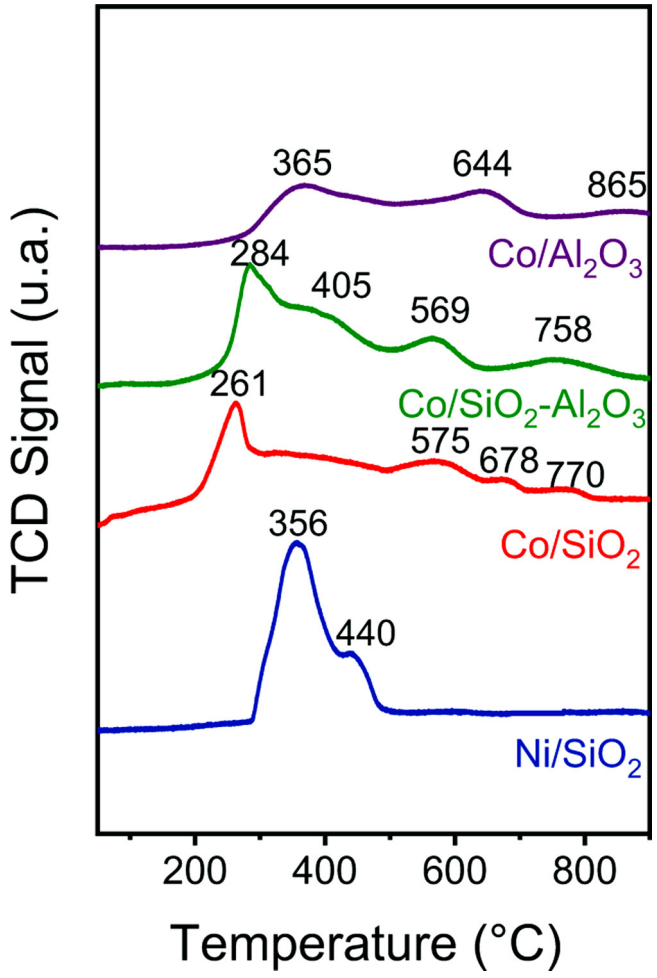

Fig. 4. Temperature-programed reduction profiles of calcined catalysts.

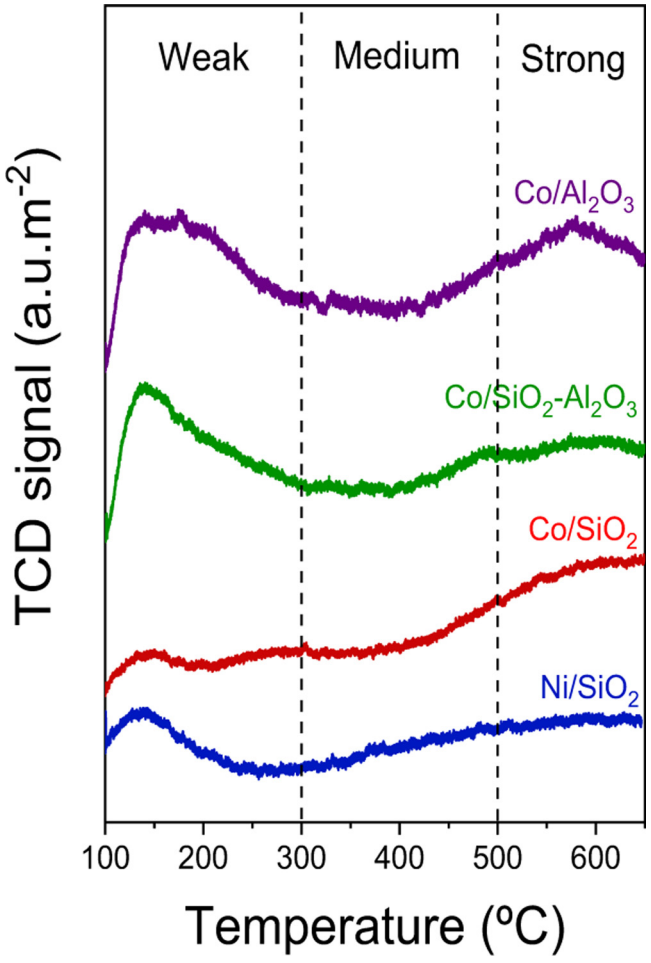

Fig. 5. TPD-NH_3 of the reduced-passivated catalysts.

Table 4
Physicochemical characterization results for all catalysts.

Catalyst	H_2 consumption[a] ($mmolg_{cat}^{-1}$)	CO uptake ($mmolg^{-1}$)	Metal disp.[b] (%)	Crystal size (nm)
Ni/SiO_2	0.814	0.02431	2.62	32
Co/SiO_2	0.301	0.01396	1.51	67
Co/SiO_2-Al_2O_3	0.032	0.00087	0.09	914
Co/Al_2O_3	0.593	0.00841	0.98	86

[a] Determined from TPR data assuming a complete reduction of oxide species to metal species of the catalysts.
[b] Calculated from CO chemisorption assuming adsorption on metal atoms only and a CO/metal = 1.5 adsorption stoichiometry.

On the other hand, Fig. 5 shows the TPD-NH_3 profile of the catalysts. According to previous reports, the strength of acid sites can be classified as a weak acid (< 300 °C), medium acid sites (300 °C < T < 500 °C), and strong acid sites (> 500 °C) [75]. Table 5 summarizes the quantified total acid sites and acid sites distribution calculated from analytical areas of deconvoluted peaks.

SiO_2 supported catalysts present mainly small peaks at the low-temperature region, indicating the predominance of weak acid sites, which are attributed to Brønsted acid sites (BAS) [54]. The Co/SiO_2-Al_2O_3 and Co/Al_2O_3 catalysts show one and two peaks respectively, Co/SiO_2-Al_2O_3 catalyst present mainly weak acid sites, assigned mainly BAS [54], whilst Co/Al_2O_3 catalyst presents both strong and weak acid sites, attributed both Lewis acid sites (LAS) and BAS [54].

The nature and the strength of acid sites have been found to play a crucial role in the catalytic conversion of biomass derivatives, like succinic acid, by influencing the intermediates of reaction and the course of the reaction [76]. In this sense, Table 3 shows that total acid sites follows the trend: Co/Al_2O_3 > Co/SiO_2-Al_2O_3 > Co/SiO_2 ≈ Ni/SiO_2.

Table 5
TPD-NH_3 results for the studied catalysts.

Catalysts	Weak acid sites (μmol $NH_3\,g^{-1}$)	Medium acid sites (μmol $NH_3\,g^{-1}$)	Strong acid sites (μmol $NH_3\,g^{-1}$)	Total acid sites (μmol $NH_3\,g^{-1}$)
Ni/SiO_2	4.9	0.5	0.7	6.1
Co/SiO_2	3.0	0.0	3.9	6.9
Co/SiO_2-Al_2O_3	16.0	0.0	3.3	19.3
Co/Al_2O_3	15.0	0.0	22.0	37.0

3.2. Theoretical results

The most stable physisorbed complexes of SA-Ni(111) and SA-Co (111) were assessed and studied by means of periodic DFT methods. Plots of the most representative complexes obtained after optimization, which correspond to the most stable ones and with the highest adsorption energy values, are presented in Figs. 6 and 7. Results indicate that the most favorable adsorption sites are those displayed in Figs. 6 and 7a with E_{ads} of -1.46 and -1.71 eV, respectively. All E_{ads} values of SA adsorption over Ni and Co metals, respectively, are summarized in Tables S1 and S2 of the supplementary data, including theoretical details.

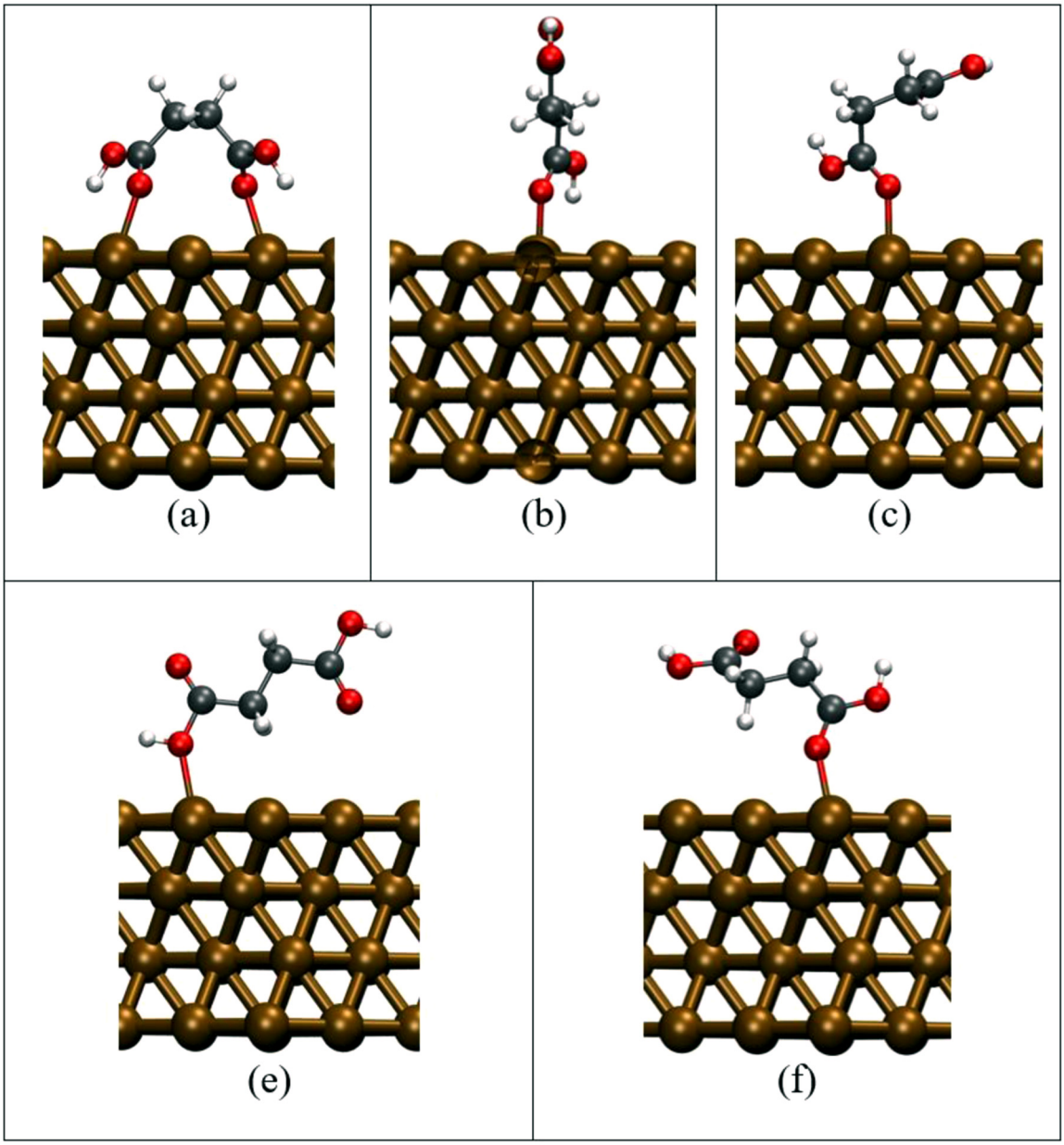

Fig. 6. Most stable adsorption complexes of SA and Ni(111), for each adsorption site. Those adsorption complexes with similar geometries were omitted.

These outcomes evidence that SA can be absorbed by the two carboxylic edges in the case of Ni, while in the case of Co, it is mostly absorbed by one carbonyl group.

3.3. Catalytic activity

Fig. 8 shows the conversion of succinic acid and the yield of products as a function of time over Ni and Co catalysts. The main product obtained over the Ni/SiO_2 catalyst was propanol (ProOH), while succinic anhydride (SAn) was produced in a minor amount. Trace amounts of γ-butyrolactone (GBL) and 2-hydroxytetrahydrofuran (THF-OH) were observed. On the other hand, the main product obtained over Co/SiO_2-Al_2O_3 and Co/Al_2O_3 catalysts was SAn, and trace amounts of ethanol (EtOH) and butanol (BuOH) for Co/SiO_2-Al_2O_3 were obtained. Meanwhile, trace amounts of THF-OH and propanal (ProAl) were obtained for Co/Al_2O_3. In the case of Co/SiO_2, there are three main products: SAn, BuOH, and butanediol (BDO) and trace amounts of GBL, ProOH, and BuOH. Additionally, Fig. 8a shows that the ProOH increase and then decrease with the time, suggesting that this is intermediary species. Similar behavior was observed to the ProAl in Fig. 8d.

Fig. 9 shows the possible ways of converting SA into different products. It is possible to observe that SAn can be obtained via dehydration (DEH) process. GBL is formed by both DEH and hydrogenation (HYD) processes. Similarly, the same process of GBL forms BDO and THF-OH. In the case of propionic acid (PA), it is formed by a decarboxylation process (DEC) of SA. Then, HYD and DEH processes from PA to form ProAl, and finally, the ProAl is HYD to ProOH. On the other hand, HYD and DEH processes from SA to form butyric acid (BA), and then BA is HYD and DEH to BuOH.

The selectivity of the catalysts is compared at 20 % of succinic acid conversion (illustrated in Fig. 10). Considering a metal effect, Ni/SiO_2 catalyst showed the selectivity mainly to propanol (ProOH), while Co/SiO_2 catalyst to BDO. These changes could not be attributed to the acidity of the catalysts, due to that these catalysts displayed similar total acidity. The substantial change in selectivity suggests that both metals have different intrinsic properties to convert the SA. In fact, the

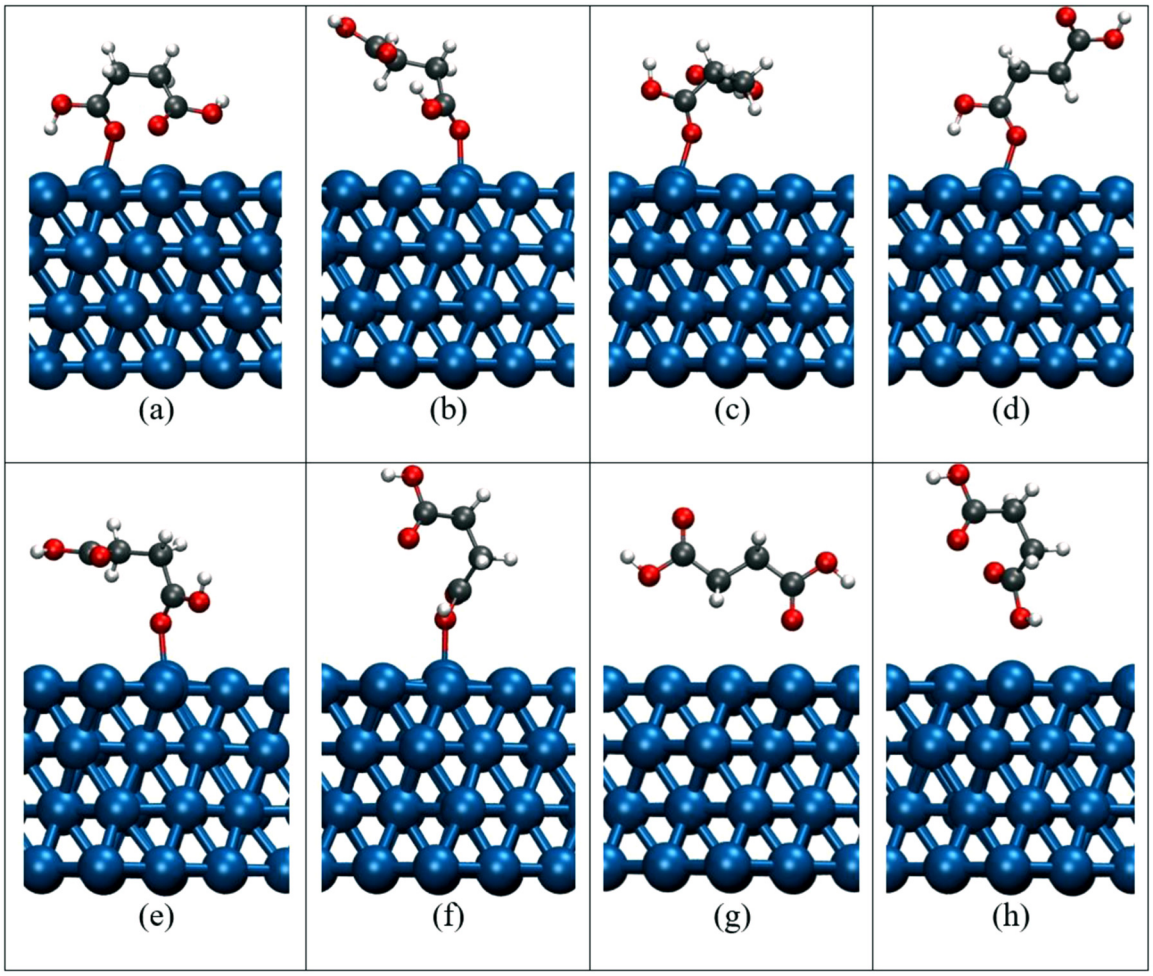

Fig. 7. Most stable adsorption complexes of SA and Co(111), for each adsorption site. Those adsorption complexes with similar geometries were omitted.

theoretical results showed different adsorption of the SA in each metal (Figs. 6 and 7a), which could be the cause of the change of selectivity. These results indicate that the Ni catalyst has the main ability to hydrogenate (HYD) and decarboxylation (DEC), while Co-based catalysts have the main property of HYD, according to the reaction scheme (Fig. 9).

On the other hand, considering the support effect of the Co catalysts, it is possible to observe in Fig. 10 that Co/SiO_2 was selective mainly to BDO, which was formed by HYD processes from SA. Meanwhile, the Co/SiO_2-Al_2O_3 catalyst produced SAn as the main compound, which was obtained by the DEH process from SA. Meanwhile, Co/Al_2O_3 catalyst shows the ProAl as the main product obtained through the DEC and HYD processes from SA.

The differences in the selectivity displayed by Co/support catalysts suggest that the active sites are different on these catalysts. The tuning of the selectivity could be attributed to the acid sites, which could be involved, together with the metal site, in the mechanism of the reaction. Wang and Huang demonstrated that acid sites favored the DEH process of the glycerol in the presence of zeolites [77]. Therefore, the highest total acidity displayed by Co/Al_2O_3 catalyst seems to favor the DEC processes, with selectivity to ProAl. On the contrary, the Co/SiO_2 catalyst has the lowest total acidity, favoring the formation of BDO through the HYD process.

Fig. 11 shows the initial rate and TOF values as a function of the catalysts. Comparing the metal effect, it is possible to observe that the Ni/SiO_2 catalyst displayed a higher initial rate than Co/SiO_2 catalyst. This behavior could be attributed to the higher dispersion of the Ni over SiO_2, (see Table 3), together with a low cobalt reduction degree, observed by XPS. On the other hand, Fig. 11 shows that Co/SiO_2 displayed the higher initial rate followed by Co/Al_2O_3 and Co/SiO_2-Al_2O_3 catalysts. This trend is no attribute to the changes in the total acidity, due to the Co/SiO_2 showed the lowest total acidity. However, this could be attributed to the Co dispersion, considering that Co/SiO_2 catalyst presented the highest Co dispersion, while Co/SiO_2-Al_2O_3 shows the lowest dispersion.

On the other hand, Fig. 11 shows that Co/SiO_2-Al_2O_3 exhibited the highest TOF value, following by Co/SiO_2 and Co/Al_2O_3 catalysts, respectively. This behavior indicates that the active sites over the Co/SiO_2-Al_2O_3 catalyst are more active than the other catalysts. The high TOF value observed to Co/SiO_2-Al_2O_3 could be attributed to the increase of the acid sites of the catalyst. This behavior suggests that in the reaction mechanism, both acid and metallic sites would be involved. On the other hand, Co/Al_2O_3 showed the highest total acidity. However, this catalyst presents the lowest TOF value. This could be due to that the highest total acid site of the Co/Al_2O_3 catalyst could favor the formation of coke, leading to deactivating the catalyst [74,78].

4. Conclusion

Ni and Co catalysts, with the same metal density content, were active in the conversion of Succinic acid. The product distribution of Ni and Co catalysts over SiO_2 showed changes of selectivity, attributed to the adsorption mode of the SA over each catalyst, determined by DFT-calculations. The SA molecules were absorbed in two active sites in the case of Ni catalyst, while in the case of Co catalysts were absorbed in one active site. On the other hand, the changes observed in the

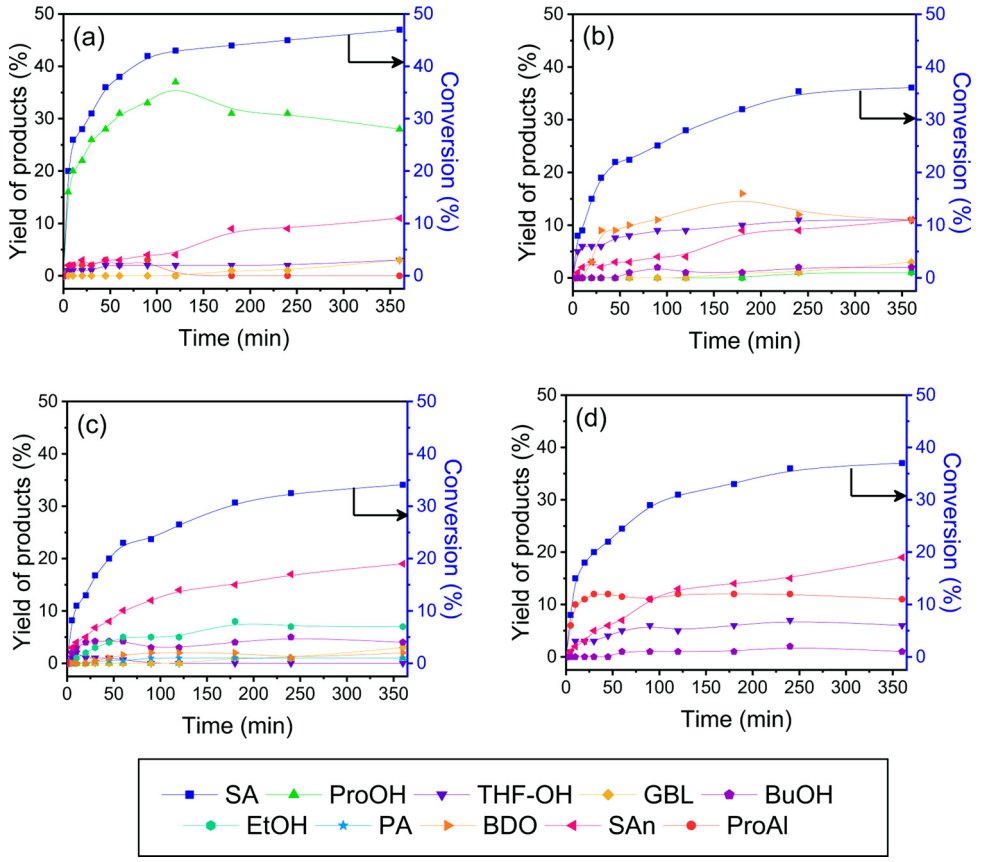

Fig. 8. Conversion of succinic acid and yield of products vs. time over: (a) Ni/SiO_2, (b) Co/SiO_2, (c) Co/SiO_2-Al_2O_3, (d) Co/Al_2O_3 catalysts.

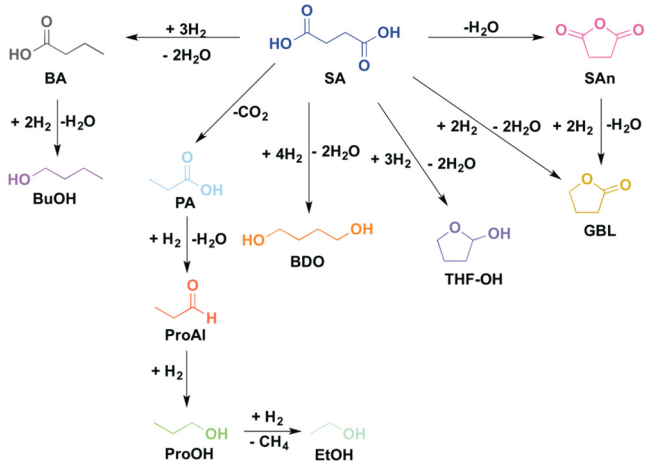

Fig. 9. Proposed reaction scheme for the succinic acid conversion.

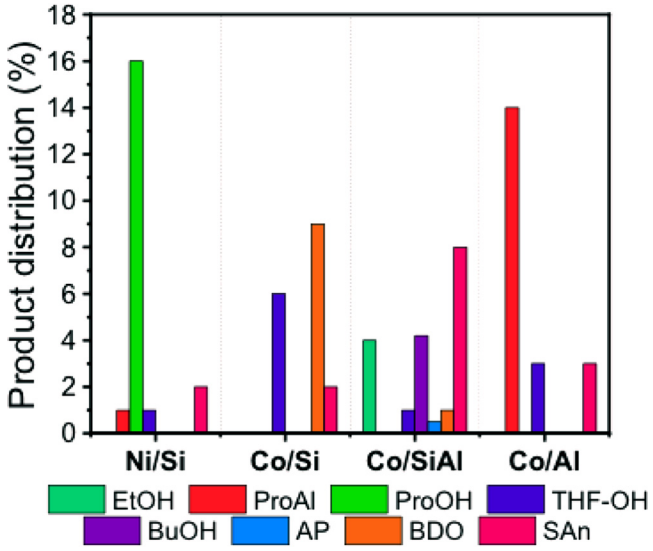

Fig. 10. Products distribution calculated at 20 % of succinic acid conversion over Ni/SiO_2 (Ni/Si), Co/SiO_2 (Co/Si), Co/SiO_2-Al_2O_3 (Co/SiAl) and Co/Al_2O_3 (Co/Al).

distribution of the product over Co/SiO_2, Co/SiO_2-Al_2O_3, and Co/Al_2O_3 catalysts were correlated with the total acidity of each catalyst, determined by TPD-NH_3. The higher acidity displayed by Co/Al_2O_3 favors the formation of ProAl by DEC and HYD; while Co/SiO_2 presented the lowest acidity, which promotes the formation of BDO and THF-OH by HYD pathway. On the other hand, the intermediate acidity displayed by Co/SiO_2-Al_2O_3 promotes the formation of SAn by DEH process.

The Ni/SiO_2 catalyst displayed the highest initial rate due to the highest metal dispersion determined by CO-Chemisorption. The same behavior was observed in the case of Co catalysts, where Co/SiO_2 shows the highest initial rate, while Co/SiO_2-Al_2O_3 shows the lowest initial rate.

The highest TOF values obtained for Co/SiO_2-Al_2O_3 suggested that the acid sites could participate in the reaction mechanism. Nevertheless, the catalyst with the highest total acidity presented the lowest TOF value, suggesting a deactivation of the active site by coke formation.

CRediT authorship contribution statement

Mabel Rojas: Conceptualization, Funding acquisition,

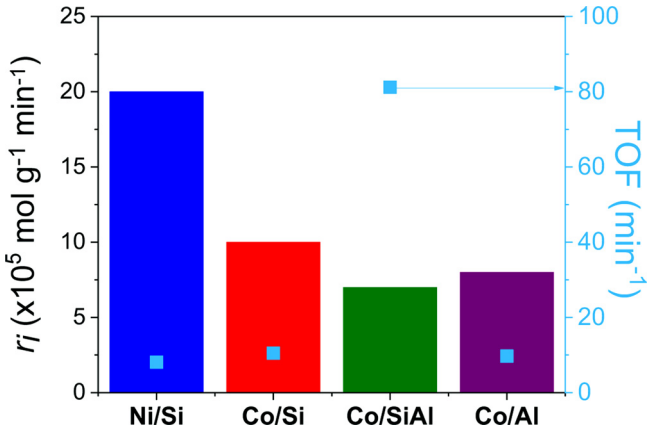

Fig. 11. Initial reaction rate and TOF values vs. catalysts.

Investigation, Methodology, Visualization, Writing - original draft. **Ximena Zarate:** Formal analysis, Writing - original draft. **Roberto I. Canales:** Visualization, Writing - review & editing. **Ana Belen Dongil:** Investigation, Resources, Writing - review & editing. **Cesar Pazo:** Investigation. **Mario Saavedra-Torres:** Formal analysis. **Néstor Escalona:** Conceptualization, Supervision, Validation, Project administration, Writing - review & editing, Funding acquisition.

Declaration of Competing Interest

The authors declare that they have no known competing financial interests or personal relationships that could have appeared to influence the work reported in this paper.

Acknowledgements

The authors gratefully acknowledge funding from the Millennium Science Initiative of the Chilean Ministry of Economy, Development and Tourism, for the grant “Nuclei on Catalytic Processes towards Sustainable Chemistry (CSC)” and Engineering School of Pontificia Universidad Católica de Chile. Additionally, funding was provided by CONICYT Chile for the following projects: PIA CCTE AFB170007 and Fondequip Nº EQM160070.

Appendix A. Supplementary data

Supplementary material related to this article can be found, in the online version, at doi:https://doi.org/10.1016/j.cattod.2020.04.067.

References

[1] G.W. Huber, S. Iborra, A. Corma, Synthesis of transportation fuels from biomass: chemistry, catalysts, and engineering, Chem. Rev. 106 (2006) 4044–4098, https://doi.org/10.1021/cr068360d.
[2] J.J. Bozell, Connecting biomass and petroleum processing with a chemical bridge, Science (80-.) 329 (2010) 522–523, https://doi.org/10.1126/science.1191662.
[3] D. Wang, B. Wang, Y. Ding, Q. Yuan, H. Wu, Y. Guan, P. Wu, Robust synthesis of green fuels from biomass-derived ethyl esters over a hierarchically core/shell-structured ZSM-5@(Co/SiO $_2$) catalyst, Chem. Commun. 53 (2017) 10172–10175, https://doi.org/10.1039/C7CC05007K.
[4] J.Q. Bond, D.M. Alonso, D. Wang, R.M. West, J. a Dumesic, Integrated catalytic conversion of g-Valerolactone to liquid alkenes for transportation fuels, Science (80-.) 327 (2010) 1110–1114, https://doi.org/10.1126/science.1184362.
[5] E.I. Gürbüz, D.M. Alonso, J.Q. Bond, J.A. Dumesic, Reactive extraction of levulinate esters and conversion to γ-Valerolactone for production of liquid fuels, ChemSusChem. 4 (2011) 357–361, https://doi.org/10.1002/cssc.201000396.
[6] M.J. Climent, A. Corma, S. Iborra, Conversion of biomass platform molecules into fuel additives and liquid hydrocarbon fuels, Green Chem. 16 (2014) 516, https://doi.org/10.1039/c3gc41492b.
[7] R.J. Van Putten, J.C. Van Der Waal, E. De Jong, C.B. Rasrendra, H.J. Heeres, J.G. De Vries, Hydroxymethylfurfural, a versatile platform chemical made from renewable resources, Chem. Rev. 113 (2013) 1499–1597, https://doi.org/10.1021/cr300182k.
[8] D.M. Alonso, S.G. Wettstein, J.A. Dumesic, Gamma-valerolactone, a sustainable platform molecule derived from lignocellulosic biomass, Green Chem. 15 (2013) 584, https://doi.org/10.1039/c3gc37065h.
[9] A.J. Ragauskas, C.K. Williams, B.H. Davison, G. Britovsek, J. Cairney, C.A. Eckert, W.J. Frederick Jr., J.P. Hallett, D.J. Leak, C.L. Liotta, J.R. Mielenz, R. Murphy, R. Templer, T. Tschaplinski, The path forward for biofuels and biomaterials, Science (80-.) 311 (2006) 484–489, https://doi.org/10.1126/science.1114736.
[10] D.M. Alonso, S.G. Wettstein, J.A. Dumesic, Bimetallic catalysts for upgrading of biomass to fuels and chemicals, Chem. Soc. Rev. 41 (2012) 8075–8098, https://doi.org/10.1039/C2CS35188A.
[11] H. Li, A. Riisager, S. Saravanamurugan, A. Pandey, R.S. Sangwan, S. Yang, R. Luque, Carbon-increasing catalytic strategies for upgrading biomass into energy-intensive fuels and chemicals, ACS Catal. 8 (2018) 148–187, https://doi.org/10.1021/acscatal.7b02577.
[12] J. Zakzeski, P.C.A. Bruijnincx, A.L. Jongerius, B.M. Weckhuysen, The catalytic valorization of ligning for the production of renewable chemicals, Chem. Rev. 110 (2010) 3552–3599, https://doi.org/10.1021/cr900354u.
[13] X. Cui, X. Zhao, D. Liu, A novel route for the flexible preparation of hydrocarbon jet fuels from biomass-based platform chemicals: a case of using furfural and 2,3-butanediol as feedstocks, Green Chem. 20 (2018) 2018–2026, https://doi.org/10.1039/C8GC00292D.
[14] M. Mascal, E.B. Nikitin, High-yield conversion of plant biomass into the key value-added feedstocks 5-(hydroxymethyl)furfural{,} levulinic acid{,} and levulinic esters via 5-(chloromethyl)furfural, Green Chem. 12 (2010) 370–373, https://doi.org/10.1039/B918922J.
[15] M.I. Alam, S. Gupta, A. Bohre, E. Ahmad, T.S. Khan, B. Saha, M.A. Haider, Development of 6-amyl-α-pyrone as a potential biomass-derived platform molecule, Green Chem. 18 (2016) 6431–6435, https://doi.org/10.1039/C6GC02528E.
[16] S. Choi, C.W. Song, J.H. Shin, S.Y. Lee, Biorefineries for the production of top building block chemicals and their derivatives, Metab. Eng. 28 (2015) 223–239, https://doi.org/10.1016/j.ymben.2014.12.007.
[17] M.J. Gilkey, B. Xu, Heterogeneous catalytic transfer hydrogenation as an effective pathway in biomass upgrading, ACS Catal. 6 (2016) 1420–1436, https://doi.org/10.1021/acscatal.5b02171.
[18] E. Lam, J.H.T. Luong, Carbon materials as catalyst supports and catalysts in the transformation of biomass to fuels and chemicals, ACS Catal. 4 (2014) 3393–3410, https://doi.org/10.1021/cs5008393.
[19] T. Werpy, G. Petersen, A. Aden, J. Bozell, J. Holladay, J. White, A. Manheim, Top Value Added Chemicals From Biomass Volume I — Results of Screening for Potential Candidates From Sugars and Synthesis Gas, (2004).
[20] J.J. Bozell, G.R. Petersen, Technology development for the production of biobased products from biorefinery carbohydrates - the US Department of Energy’s “top 10” revisited, Green Chem. 12 (2010) 539–554, https://doi.org/10.1039/b922014c.
[21] M. Sauer, D. Porro, D. Mattanovich, P. Branduardi, Microbial production of organic acids: expanding the markets, Trends Biotechnol. 26 (2008) 100–108, https://doi.org/10.1016/j.tibtech.2007.11.006.
[22] M. Jiang, J. Ma, M. Wu, R. Liu, L. Liang, F. Xin, W. Zhang, H. Jia, W. Dong, Progress of succinic acid production from renewable resources: metabolic and fermentative strategies, Bioresour. Technol. 245 (2017) 1710–1717, https://doi.org/10.1016/j.biortech.2017.05.209.
[23] M.L.A. Jansen, W.M. van Gulik, Towards large scale fermentative production of succinic acid, Curr. Opin. Biotechnol. 30 (2014) 190–197, https://doi.org/10.1016/j.copbio.2014.07.003.
[24] G.T. Hermanson, Bioconjugate Techniques, 3rd ed., Academic Press, London, 2013.
[25] P.-C. Chang, H.-Y. Hsu, G.-W. Jang, Biological routes to itaconic and succinic acids, Phys. Sci. Rev. 1 (2016) 1–17, https://doi.org/10.1515/psr-2016-0052.
[26] R.K. Saxena, S. Saran, J. Isar, R. Kaushik, 27. Production and applications of succinic acid, in: A. Pandey, S. Negi, C.R. Soccol (Eds.), Curr. Dev. Biotechnol. Bioeng. Elsevier, 2017, pp. 601–630, , https://doi.org/10.1016/B978-0-444-63662-1.00027-0.
[27] C. Delhomme, D. Weuster-Botz, F.E. Kühn, Succinic acid from renewable resources as a C_4 building-block chemical—a review of the catalytic possibilities in aqueous media, Green Chem. 11 (2009) 13–26, https://doi.org/10.1039/B810684C.
[28] Ana Cukalovic, Christian V. Stevens, Feasibility of production methods for succinic acid derivatives: a marriage of renewable resources and chemical technology, Biofuels, Bioprod. Biorefining 2 (2008) 505–529, https://doi.org/10.1002/bbb.
[29] B. Kamm, M. Kamm, Biorefineries - multi product processes, in: R. Ulber, D. Sell (Eds.), White Biotechnol. Springer Berlin Heidelberg, Berlin, Heidelberg, 2007, pp. 175–204, , https://doi.org/10.1007/10_2006_040.
[30] M.E. Bertone, C.I. Meyer, S.A. Regenhardt, V. Sebastian, T.F. Garetto, A.J. Marchi, Highly selective conversion of maleic anhydride to γ-butyrolactone over Ni-supported catalysts prepared by precipitation-deposition method, Appl. Catal. A Gen. 503 (2015) 135–146, https://doi.org/10.1016/j.apcata.2015.07.013.
[31] R. Luque, J.H. Clark, K. Yoshida, P.L. Gai, Efficient aqueous hydrogenation of biomass platform molecules using supported metal nanoparticles on Starbons®, Chem. Commun. 5305 (2009), https://doi.org/10.1039/b911877b.
[32] X. Di, C. Li, G. Lafaye, C. Especel, F. Epron, C. Liang, Influence of Re-M interactions in Re-M/C bimetallic catalysts prepared by a microwave-assisted thermolytic method on aqueous-phase hydrogenation of succinic acid, Catal. Sci. Technol. 7 (2017) 5212–5223, https://doi.org/10.1039/c7cy01039g.
[33] R.M. Deshpande, V.V. Buwa, C.V. Rode, R.V. Chaudhari, P.L. Mills, Tailoring of activity and selectivity using bimetallic catalyst in hydrogenation of succinic acid, Catal. Commun. 3 (2002) 269–274, https://doi.org/10.1016/S1566-7367(02)00119-X.
[34] K.H. Kang, S.J. Han, J.W. Lee, T.H. Kim, I.K. Song, Effect of boron content on 1,4-

butanediol production by hydrogenation of succinic acid over Re-Ru/BMC (boron-modified mesoporous carbon) catalysts, Appl. Catal. A Gen. 524 (2016) 206–213, https://doi.org/10.1016/j.apcata.2016.06.037.
[35] Y. Takeda, M. Tamura, Y. Nakagawa, K. Okumura, K. Tomishige, Hydrogenation of dicarboxylic acids to diols over Re-Pd catalysts, Catal. Sci. Technol. 6 (2016) 5668–5683, https://doi.org/10.1039/c6cy00335d.
[36] B. Tapin, F. Epron, C. Especel, B.K. Ly, C. Pinel, M. Besson, Study of monometallic Pd/TiO2 catalysts for the hydrogenation of succinic acid in aqueous phase, ACS Catal. 3 (2013) 2327–2335.
[37] J.C. Serrano-Ruiz, R. Luque, A. Sepúlveda-Escribano, Transformations of biomass-derived platform molecules: from high added-value chemicals to fuels via aqueous-phase processing, Chem. Soc. Rev. 40 (2011) 5266, https://doi.org/10.1039/c1cs15131b.
[38] K.H. Kang, U.G. Hong, Y. Bang, J.H. Choi, J.K. Kim, J.K. Lee, S.J. Han, I.K. Song, Hydrogenation of succinic acid to 1,4-butanediol over Re-Ru bimetallic catalysts supported on mesoporous carbon, Appl. Catal. A Gen. 490 (2015) 153–162, https://doi.org/10.1016/j.apcata.2014.11.029.
[39] I. Bechthold, K. Bretz, S. Kabasci, R. Kopitzky, A. Springer, Succinic acid: a new platform chemical for biobased polymers from renewable resources, Chem. Eng. Technol. 31 (2008) 647–654, https://doi.org/10.1002/ceat.200800063.
[40] P. Gallezot, Conversion of biomass to selected chemical products, Chem. Soc. Rev. 41 (2012) 1538–1558, https://doi.org/10.1039/C1CS15147A.
[41] U.G. Hong, S. Hwang, J.G. Seo, J. Lee, I.K. Song, Hydrogenation of succinic acid to γ-butyrolactone (GBL) over palladium catalyst supported on alumina xerogel: effect of acid density of the catalyst, J. Ind. Eng. Chem. 17 (2011) 316–320, https://doi.org/10.1016/j.jiec.2011.02.030.
[42] S.H. Chung, Y.M. Park, M.S. Kim, K.Y. Lee, The effect of textural properties on the hydrogenation of succinic acid using palladium incorporated mesoporous supports, Catal. Today 185 (2012) 205–210, https://doi.org/10.1016/j.cattod.2011.08.011.
[43] U.G. Hong, H.W. Park, J. Lee, S. Hwang, I.K. Song, Hydrogenation of succinic acid to γ-butyrolactone (GBL) over ruthenium catalyst supported on surfactant-templated mesoporous carbon, J. Ind. Eng. Chem. 18 (2012) 462–468, https://doi.org/10.1016/j.jiec.2011.11.054.
[44] U.G. Hong, J.K. Kim, J. Lee, J.K. Lee, J.H. Song, J. Yi, I.K. Song, Hydrogenation of succinic acid to tetrahydrofuran (THF) over ruthenium-carbon composite (Ru-C) catalyst, Appl. Catal. A Gen. 469 (2014) 466–471, https://doi.org/10.1016/j.apcata.2013.10.029.
[45] U.G. Hong, H.W. Park, J. Lee, S. Hwang, J. Yi, I.K. Song, Hydrogenation of succinic acid to tetrahydrofuran (THF) over rhenium catalyst supported on H2SO4-treated mesoporous carbon, Appl. Catal. A Gen. 415–416 (2012) 141–148, https://doi.org/10.1016/j.apcata.2011.12.022.
[46] U.G. Hong, J.K. Kim, J. Lee, J.K. Lee, J.H. Song, J. Yi, I.K. Song, Hydrogenation of succinic acid to tetrahydrofuran over ruthenium-carbon composite catalysts: effect of HCl concentration in the preparation of the catalysts, J. Ind. Eng. Chem. 20 (2014) 3834–3840, https://doi.org/10.1016/j.jiec.2013.12.087.
[47] C. Zhang, L. Chen, H. Cheng, X. Zhu, Z. Qi, Atomically dispersed Pd catalysts for the selective hydrogenation of succinic acid to Γ-butyrolactone, Catal. Today 276 (2016) 55–61, https://doi.org/10.1016/j.cattod.2016.01.028.
[48] K. Yakabi, A. Jones, A. Buchard, A. Roldan, C. Hammond, Chemoselective lactonization of renewable succinic acid with heterogeneous nanoparticle catalysts, ACS Sustain. Chem. Eng. 6 (2018) 16341–16351, https://doi.org/10.1021/acssuschemeng.8b03346.
[49] S.D. Le, S. Nishimura, K. Ebitani, Direct esterification of succinic acid with phenol using zeolite beta catalyst, Catal. Commun. 122 (2019) 20–23, https://doi.org/10.1016/j.catcom.2019.01.006.
[50] M. Abou Hamdan, S. Loridant, M. Jahjah, C. Pinel, N. Perret, TiO2-supported molybdenum carbide: an active catalyst for the aqueous phase hydrogenation of succinic acid, Appl. Catal. A Gen. 571 (2019) 71–81, https://doi.org/10.1016/j.apcata.2018.11.009.
[51] S.D. Le, S. Nishimura, Highly selective synthesis of 1,4-butanediol via hydrogenation of succinic acid with supported Cu–Pd alloy nanoparticles, ACS Sustain. Chem. Eng. 7 (2019) 18483–18492, https://doi.org/10.1021/acssuschemeng.9b04447.
[52] V. Humblot, M.O. Lorenzo, C.J. Baddeley, S. Haq, R. Raval, Local and global chirality at surfaces: succinic acid versus tartaric acid on Cu(110), J. Am. Chem. Soc. 126 (2004) 6460–6469, https://doi.org/10.1021/ja0382056.
[53] P. Taheri, T. Hauffman, J.M.C. Mol, J.R. Flores, F. Hannour, J.H.W. de Wit, H. Terryn, Molecular interactions of electroadsorbed carboxylic acid and succinic anhydride monomers on zinc surfaces, J. Phys. Chem. C 115 (2011) 17054–17067, https://doi.org/10.1021/jp204751z.
[54] I.T. Ghampson, C. Sepúlveda, A.B. Dongil, G. Pecchi, R. García, J.L.G. Fierro, N. Escalona, Phenol hydrodeoxygenation: effect of support and Re promoter on the reactivity of Co catalysts, Catal. Sci. Technol. (2016) 7289–7306, https://doi.org/10.1039/c6cy01038e.
[55] J. Gross, G. Sadowski, Perturbed-chain SAFT: an equation of state based on a perturbation theory for chain molecules, Ind. Eng. Chem. Res. 40 (2001) 1244–1260, https://doi.org/10.1021/ie0003887.
[56] E. Brunner, Solubility of hydrogen in 10 organic solvents at 298.15, 323.15, and 373.15 K, J. Chem. Eng. Data 30 (1985) 269–273, https://doi.org/10.1021/je00041a010.
[57] N. Vogt, M.A. Abaev, A.N. Rykov, I.F. Shishkov, Determination of molecular structure of succinic acid in a very complex conformational landscape: gas-phase electron diffraction (GED) and ab initio studies, J. Mol. Struct. 996 (2011) 120–127, https://doi.org/10.1016/j.molstruc.2011.04.034.
[58] J.D. Roberts, Fascination with the conformational analysis of succinic acid, as evaluated by NMR spectroscopy, and why, Acc. Chem. Res. 39 (2006) 889–896, https://doi.org/10.1021/ar050229p.
[59] R. Lizárraga, F. Pan, L. Bergqvist, E. Holmström, Z. Gercsi, L. Vitos, First principles theory of the hcp-fcc phase transition in cobalt, Sci. Rep. 7 (2017) 6–13, https://doi.org/10.1038/s41598-017-03877-5.
[60] V.A. de la Peña O'Shea, I.P.R. de Moreira, A. Roldán, F. Illas, Electronic and magnetic structure of bulk cobalt: the α, B, and ε -phases from density functional theory calculations, J. Chem. Phys. 133 (2010), https://doi.org/10.1063/1.3458691.
[61] A. Gulans, S. Kontur, T.R. Measurements, Advanced capabilities for materials modelling with Quantum ESPRESSO, J. Phys. Condend. Matter. 29 (2017) 465901.
[62] P. Giannozzi, S. Baroni, N. Bonini, M. Calandra, R. Car, C. Cavazzoni, D. Ceresoli, G.L. Chiarotti, M. Cococcioni, I. Dabo, A. Dal Corso, S. De Gironcoli, S. Fabris, G. Fratesi, R. Gebauer, U. Gerstmann, C. Gougoussis, A. Kokalj, M. Lazzeri, L. Martin-Samos, N. Marzari, F. Mauri, R. Mazzarello, S. Paolini, A. Pasquarello, L. Paulatto, C. Sbraccia, S. Scandolo, G. Sclauzero, A.P. Seitsonen, A. Smogunov, P. Umari, R.M. Wentzcovitch, QUANTUM ESPRESSO: a modular and open-source software project for quantum simulations of materials, J. Phys. Condens. Matter 21 (2009), https://doi.org/10.1088/0953-8984/21/39/395502.
[63] J.P. Perdew, K. Burke, M. Ernzerhof, Generalized gradient approximation made simple, Phys. Rev. Lett. 77 (1996) 3865–3868, https://doi.org/10.1103/PhysRevLett.77.3865.
[64] A. Dal Corso, Pseudopotentials periodic table: from H to Pu, Comput. Mater. Sci. 95 (2014) 337–350, https://doi.org/10.1016/j.commatsci.2014.07.043.
[65] S. Jin, Z. Xiao, C. Li, X. Chen, L. Wang, J. Xing, W. Li, C. Liang, Catalytic hydrodeoxygenation of anisole as lignin model compound over supported nickel catalysts, Catal. Today 234 (2014) 125–132, https://doi.org/10.1016/j.cattod.2014.02.014.
[66] M. Zhou, J. Ye, P. Liu, J. Xu, J. Jiang, Water-assisted selective hydrodeoxygenation of guaiacol to cyclohexanol over supported Ni and Co bimetallic catalysts, ACS Sustain. Chem. Eng. 5 (2017) 8824–8835, https://doi.org/10.1021/acssuschemeng.7b01615.
[67] K. Schumacher, M. Grün, K.K. Unger, Novel synthesis of spherical MCM-48, Microporous Mesoporous Mater. 27 (1999) 201–206, https://doi.org/10.1016/S1387-1811(98)00254-6.
[68] M. Zhou, L. Tian, L. Niu, C. Li, G. Xiao, R. Xiao, Upgrading of liquid fuel from fast pyrolysis of biomass over modified Ni/CNT catalysts, Fuel Process. Technol. 126 (2014) 12–18, https://doi.org/10.1016/j.fuproc.2014.04.015.
[69] S.V. Klokov, E.S. Lokteva, E.V. Golubina, P.A. Chernavskii, K.I. Maslakov, T.B. Egorova, S.A. Chernyak, A.S. Minin, A.S. Konev, Cobalt–carbon nanocomposite catalysts of gas-phase hydrodechlorination of chlorobenzene, Appl. Surf. Sci. 463 (2019) 395–402, https://doi.org/10.1016/j.apsusc.2018.08.105.
[70] W. Chu, P.A. Chernavskii, L. Gengembre, G.A. Pankina, P. Fongarland, A.Y. Khodakov, Cobalt species in promoted cobalt alumina-supported Fischer-Tropsch catalysts, J. Catal. 252 (2007) 215–230, https://doi.org/10.1016/j.jcat.2007.09.018.
[71] Y. Liu, L. Jia, B. Hou, D. Sun, D. Li, Cobalt aluminate-modified alumina as a carrier for cobalt in Fischer–Tropsch synthesis, Appl. Catal. A Gen. 530 (2017) 30–36, https://doi.org/10.1016/j.apcata.2016.11.014.
[72] A.Y. Khodakov, W. Chu, P. Fongarland, Advances in the development of novel cobalt Fischer-Tropsch catalysts for synthesis of long-chain hydrocarbons and clean fuels, Chem. Rev. 107 (2007) 1692–1744, https://doi.org/10.1021/cr050972v.
[73] A.B. Dongil, I.T. Ghampson, R. García, J.L.G. Fierro, N. Escalona, Hydrodeoxygenation of guaiacol over Ni/carbon catalysts: effect of the support and Ni loading, RSC Adv. 6 (2016) 2611–2623, https://doi.org/10.1039/c5ra22540j.
[74] M.V. Bykova, D.Y. Ermakov, V.V. Kaichev, O.A. Bulavchenko, A.A. Saraev, M.Y. Lebedev, V. Yakovlev, Ni-based sol-gel catalysts as promising systems for crude bio-oil upgrading: guaiacol hydrodeoxygenation study, Appl. Catal. B Environ. 113–114 (2012) 296–307, https://doi.org/10.1016/j.apcatb.2011.11.051.
[75] R. Nava, B. Pawelec, P. Castaño, M.C. Álvarez-Galván, C.V. Loricera, J.L.G. Fierro, Upgrading of bio-liquids on different mesoporous silica-supported CoMo catalysts, Appl. Catal. B Environ. 92 (2009) 154–167, https://doi.org/10.1016/j.apcatb.2009.07.014.
[76] X. Liu, X. Wang, G. Xu, Q. Liu, X. Mu, H. Liu, Tuning the catalytic selectivity in biomass-derived succinic acid hydrogenation on FeOx-modified Pd catalysts, J. Mater. Chem. A 3 (2015) 23560–23569, https://doi.org/10.1039/c5ta03843j.
[77] Z. Wang, L. Wang, Y. Jiang, M. Hunger, J. Huang, Cooperativity of Brønsted and lewis acid sites on zeolite for glycerol dehydration, ACS Catal. 4 (2014) 1144–1147, https://doi.org/10.1021/cs401225k.
[78] I.T. Ghampson, C. Sepúlveda, R. Garcia, L.R. Radovic, J.L.G. Fierro, W.J. Desisto, N. Escalona, Hydrodeoxygenation of guaiacol over carbon-supported molybdenum nitride catalysts: effects of nitriding methods and support properties, Appl. Catal. A Gen. 439–440 (2012) 111–124, https://doi.org/10.1016/j.apcata.2012.06.047.